

## Article

## A Kinetic Study of Ovalbumin Fibril Formation: The Importance of Fragmentation and End-Joining

Jason M. D. Kalapothakis,<sup>1,2</sup> Ryan J. Morris,<sup>1</sup> Juraj Szavits-Nossan,<sup>1</sup> Kym Eden,<sup>1</sup> Sam Covill,<sup>1</sup> Sean Tabor,<sup>1</sup> Jay Gillam,<sup>1</sup> Perdita E. Barran,<sup>3</sup> Rosalind J. Allen,<sup>1</sup> and Cait E. MacPhee<sup>1,\*</sup>

<sup>1</sup>School of Physics and Astronomy and <sup>2</sup>School of Chemistry, University of Edinburgh, Edinburgh, UK; and <sup>3</sup>School of Chemistry, The University of Manchester, Manchester, UK

**ABSTRACT** The ability to control the morphologies of biomolecular aggregates is a central objective in the study of self-assembly processes. The development of predictive models offers the surest route for gaining such control. Under the right conditions, proteins will self-assemble into fibers that may rearrange themselves even further to form diverse structures, including the formation of closed loops. In this study, chicken egg white ovalbumin is used as a model for the study of fibril loops. By monitoring the kinetics of self-assembly, we demonstrate that loop formation is a consequence of end-to-end association between protein fibrils. A model of fibril formation kinetics, including end-joining, is developed and solved, showing that end-joining has a distinct effect on the growth of fibrillar mass density (which can be measured experimentally), establishing a link between self-assembly kinetics and the underlying growth mechanism. These results will enable experimentalists to infer fibrillar morphologies from an appropriate analysis of self-assembly kinetic data.

### INTRODUCTION

The self-assembly of polypeptides into fibrillar aggregates is relevant into areas as diverse as disease pathology (1) and the synthesis of biocompatible nanomaterials (2,3). The formation of amyloid-like fibrils, which are rich in  $\beta$ -sheet structure, has been the focus of much research due to the universal nature of the self-assembly process: most if not all proteins can form amyloid-like fibrils under appropriate (not necessarily physiological) environmental conditions (4). The kinetics of amyloid fibril formation can be tracked using  $\beta$ -sheet-binding dyes such as Congo Red or Thioflavin T (Th T) or monitoring turbidity, while the morphology of the resulting fibrils can be assessed using electron microscopy. However, these are usually measured in separate studies—few attempts have been made to link self-assembly kinetics to fibril morphology. Establishing such a link would be an important step forward in understanding, predicting, and controlling protein aggregation processes.

The kinetics of amyloid-like fibril formation, as measured using spectroscopic assays such as the thioflavin T fluorescence assay (5–7), are typically characterized by growth curves of a sigmoidal or sigmoidal-like form, in which a quiescent lag phase—often lasting hours or even days—is followed by rapid growth, culmi-

nating in a plateau when monomeric protein is exhausted or the system reaches equilibrium. The lag phase can be abolished by adding preformed fibril seeds, suggesting that a nucleation process plays a key role. Indeed, theoretical models that include nucleation, growth by monomer addition at fibril ends, and autocatalysis via fibril fragmentation, can successfully reproduce these sigmoidlike growth curves (8–10). Here the role of fibril fragmentation is to form new growth-competent fibril ends that accelerate the depletion of monomer during the growth phase, leading to the characteristic sigmoidal form for the fibril growth curve. These models also predict characteristic scaling laws for the lag time and maximal growth rate as functions of the protein concentration. An alternative protein aggregation process may exhibit rapid fibril growth from the very onset, with an absence of lag phase—examples of this phenomenon are cited below.

Amyloid fibrils have been observed to form in a wide variety of morphologies, including long rigid fibrils, short rodlike forms, tapes, twisted ribbons, nanotubes, and flexible wormlike chains that are characterized by a short persistence length (1,11–17). Fibril polymorphism may become manifest when the self-assembly takes place under different conditions, as seen for  $\beta$ 2-microglobulin (18), or, alternatively, two forms may arise simultaneously, as observed for amyloid  $\beta$  (19,20). Intriguingly, a number of systems that form fibers with wormlike chains have also been observed to form ring or loop structures (e.g., apolipoprotein C-II (21),  $\alpha$ -synuclein (22), the crystallins

Submitted October 7, 2014, and accepted for publication March 12, 2015.

\*Correspondence: [cait.macphee@ed.ac.uk](mailto:cait.macphee@ed.ac.uk)

J. M. D. Kalapothakis, R. J. Morris, and J. Szavits-Nossan contributed equally to this work.

Editor: Elizabeth Rhoades.

© 2015 by the Biophysical Society  
0006-3495/15/05/2300/12 \$2.00

<http://dx.doi.org/10.1016/j.bpj.2015.03.021>



(23,24), human serum albumin (25),  $\beta$ -lactoglobulin (26), and  $\alpha$ <sub>S2</sub>-casein (27)). The simplest hypothesis for the formation of loops by protein fibrils is the joining of their two ends (28). This hypothesis implies a link to fibril growth kinetics, because end-joining decreases the number of fibril ends available for growth by monomer addition. In this study, we show that such a link between end-joining and self-assembly kinetics indeed exists, using the 44.5-kDa glycoprotein OVA, the main protein component of avian egg white, as a model system. Due to its abundance, OVA is a convenient model system for the study of fibril formation. Under acidic or near-neutral conditions ( $\text{pH} \leq 7$ ) and elevated temperatures, OVA forms fibrils that display amyloid-like behavior in that they bind the dyes Th T and Congo Red (29–33) (Fig. 3 and Figs. S1 and S2 in the Supporting Material). The formation of amyloid-like fibrils is more pronounced when the reaction takes place in a reducing environment (34). Published images of OVA fibers indicate flexible morphologies (32), but under reducing conditions, more rigid fibers have also been observed (34). We investigate in detail the self-assembly kinetics of OVA fibrils, under conditions where flexible fibrils, with some closed loops, are formed. We develop a theoretical model that includes both fibril fragmentation and the joining of fibril ends. By fitting our model to our experimental data, we show that both fragmentation and end-joining play important roles in the self-assembly kinetics.

## MATERIALS AND METHODS

### Preparation of ovalbumin fibrils

Ovalbumin (isolated from chicken egg white) was used in this study (Grade 5, A5503; Sigma, St. Louis, MO). To produce reduced OVA samples, the lyophilized protein powder was dissolved in aqueous 10 mM ammonium acetate, 10 mM DTT (dithiothreitol) buffer ( $\text{pH}$  6.8), achieving the desired protein concentrations (ranging between 0.1 and 12.8 mg/mL). Subsequently, the sample, distributed in 1.2 mL aliquots in Eppendorf tubes secured with parafilm, was incubated on a benchtop block heater at 37°C for 2 h. Reduced protein aliquots were mixed, cooled on ice, and filtered with a 200-nm cutoff filter. Fibrils were produced by incubating the samples at 60°C. Incubation typically occurred in 96-well plates in the plate reader or on the block heater (in the latter case, Eppendorf tubes were secured with parafilm).

### Thioflavin T fluorescence kinetics at 60°C

Fibril formation kinetics were followed by means of the Th T fluorescence assay. Th T was added to reduced protein samples to a concentration of 55  $\mu\text{M}$ . Aliquots of 100  $\mu\text{L}$  were added in 96-well plates. Nonbinding surface plates (coated with a PEG-like polymer; Corning Incorporated, Corning, NY) and Nunc-Immuno StarWell Modules (PolySorp surface, polystyrene coating; Nunc Products, Thermo Fisher Scientific, Guilford, CT), the latter sealed with polyethylene caps, were used for these experiments. Both plate types were sealed additionally with a transparent adhesive Greiner plate sealer and secured further with parafilm to minimize solvent evaporation. Typically 60 out of a total of 96 wells

contained the protein solution with the remaining 36 being used for blanks. The kinetics were measured using a Synergy 2 plate reader (BioTek, Winooski, VT). The microplate was kept at a temperature of 60°C for plate-reader measurements. Th T fluorescence readings ( $\lambda_{\text{exc}} = 440$  nm,  $\lambda_{\text{em}} = 485$  nm) were collected every 8 min, with an 18-Hz shaking frequency (at medium setting). Th T binding kinetics were probed for 3–5 days.

### Temperature-dependence of Th T binding kinetics

The kinetics of Th T binding were measured on quiescent samples on a Cary Eclipse fluorimeter, fitted with a Peltier device (Varian, Cary, NC). A 3.0 mL quantity of 6.0 mg/mL reduced protein solution (prepared as described above) was added to 10-mm-path quartz cuvettes (Starna Scientific, Hainault, Essex, UK). The kinetics were monitored for 24 h, collecting a reading every 10 min. OVA Th T binding kinetics were measured at 50, 55, 60, 65, 70, and 80°C in this fashion. These experiments were repeated in triplicate, with buffer blanks being measured in duplicate.

### Transmission electron microscopy

For transmission electron microscopy (TEM), 2.0  $\mu\text{L}$  of a reduced OVA fibril suspension was deposited on formvar/carbon-coated TEM grids (TAAB Laboratories Equipment, Aldermaston, Berkshire, UK). The sample was allowed to equilibrate for 5 min, after which the excess was removed with a filter paper wedge and washed with 20  $\mu\text{L}$  of distilled H<sub>2</sub>O, which was then immediately removed. The samples were stained with 1% w/v uranyl acetate. Staining time ranged between 30 and 45 s. Excess stain was removed and the grids were allowed to dry for at least 20 min before analysis.

TEM images were collected on a CM 120 Philips BioTwin transmission electron microscope operating at an accelerating voltage of 80 kV (FEI, Hillsboro, OR). Images were captured by an Orius 1000 charge-coupled device camera (Gatan, Pleasanton, CA) controlled using DIGITALMICROGRAPH (Gatan) imaging software. Image analysis was carried out using the IMAGEJ program (National Institutes of Health, Bethesda, MD).

### Protein quantitation

Whenever necessary, protein concentrations were determined using the Bradford assay. A quantity of 10  $\mu\text{L}$  of standard protein solution or fibril sample (appropriately diluted—1, 2, 5, or 10 $\times$ —in 10 mM NH<sub>4</sub>CH<sub>3</sub>COO 10 mM DTT buffer) was dissolved in 200  $\mu\text{L}$  of Bradford reagent. The absorbance was recorded at 450 and 595 nm and the ratio of the two readings was used to construct the standard curve and to determine the concentrations. OVA was used as the protein standard, allowing accurate concentration determination.

### Model for fibril formation by linear growth, end-joining, and fragmentation

Our kinetic and morphological observations, presented in Results and Discussion, suggest that OVA fibril formation involves seeded linear fibril growth, combined with a secondary process, such as end-to-end joining, that can produce loops. Indeed, a kinetic model that includes seeded linear growth and end-joining (which can be solved analytically; see the Supporting Material) does predict rapid fibril growth followed by saturation, similar to what we see in our experiments. However, this model does not reproduce the slower growth regime we observe that follows the rapid growth regime. When fragmentation is included, three growth phases

arise: an initial rapid elongation, followed by continued but slower growth, which eventually reaches a steady state (Fig. S10). In the absence of fragmentation, the rapid initial growth is followed by transition to the steady state, and the slower growth regime is absent (Fig. S10). We find the experimental data is best fit to a model that includes fibril fragmentation—i.e., the generation of new fibril ends by breakage of growing fibrils (see Figs. 3 and 6). This suggests that fragmentation is a significant factor in the self-assembly of OVA, even though its growth kinetics display none of the characteristics typically associated with fragmentation-based models.

A model for the self-assembly of fibrils that incorporates end-joining and loop formation can be summarized using the following reaction set, schematically presented in Fig. 1:

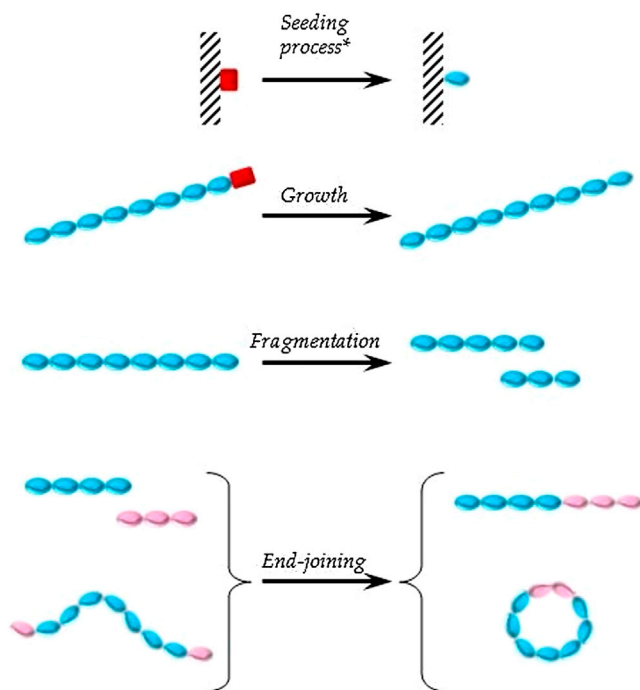
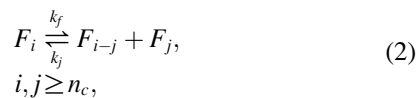
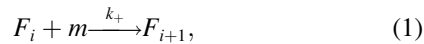


FIGURE 1 Schematic representation of processes described by Eqs. 1–3. These processes are thought to take place during OVA self-assembly. The process giving rise to the initial seed population is not defined explicitly and instead is modeled by the presence of a seed population that forms rapidly at early times. We suggest, however, that for ovalbumin, seeding occurs at interfaces (e.g., the air/water interface and/or the walls of the container) represented schematically (hashed bars). (Red square) Monomer protein units; (blue and pink ovals) active nuclei and fibrillar units. Three processes are active during fibril formation: elongation, fragmentation, and end-joining. Two consequences of end-joining are illustrated: fibril concatenation and loop-formation. To see this figure in color, go online.

Here,  $F_i$  is a single fibril of length  $i$ ,  $m$  is a single monomer,  $n_c$  is the number of monomers in the smallest stable fibril (fibrils shorter than  $n_c$  are assumed to dissolve into monomers), and  $F_i^{\text{loop}}$  is a loop of size  $i$ . The total monomer concentration is denoted with  $m(t)$ . The first reaction describes the elongation of a fibril by addition of a monomer to either of its ends, with rate constant  $k_+$ . The second reaction describes the breakage of a fibril of length  $i$  at any point between two of its monomers with rate constant  $k_f$ ; the opposite process of joining two fibril ends has rate constant  $k_j$ . The third reaction describes the breakage of a loop of length  $i$  in a similar way to that of a single fibril (note: a loop contains one more breakable bond than a fibril of the same length) with the same rate constant  $k_f$ ; similarly, in the opposite process a loop is formed with rate constant  $k_j$ ; this rate is given by  $k_j/V$  (where  $V$  is volume) multiplied by the probability  $P_{\text{loop}}$  of two ends of a wormlike chain coming together (21). In our study, to a first approximation, we take  $k_j$  and  $k_l$  to be of the same magnitude and it should be noted that  $k_j$  and  $k_+$  are an intrinsic property of any given fibril-forming system and may depend on the structural characteristics of the aggregating protein.

The rate equations for the mass density  $M(t)$  and the number density  $N(t)$  of fibrils may be written as

$$\frac{dM}{dt} = 2k_+(m_{\text{tot}} - M)N - k_f n_c (n_c - 1)N, \quad (4)$$

$$M(0) = M_0,$$

$$\frac{dN}{dt} = k_f [M - (2n_c - 1)N] - k_j N^2, \quad (5)$$

$$N(0) = N_0,$$

where  $m_{\text{tot}}$  represents the total density of protein monomers, and  $N_0$  and  $M_0$  are the initial (seed) fibril number density and the fibril mass concentration, respectively. Equations 4 and 5 were derived from the master equation for the number density of fibrils of sizes  $i \geq n_c$ , where, to the first approximation, we ignored the contributions to  $M$  and  $N$  from loops (see the Supporting Material).

Solving for the steady state of the set of Eqs. 4 and 5 provides an expression for the fibril mass concentration  $M^*$  and number density  $N^*$ , in the long-time limit:

$$M^* = m_{\text{tot}} - \frac{k_f n_c (n_c - 1)}{2k_+}, \quad (6)$$

$$N^* = \frac{\sqrt{k_f^2 (2n_c - 1)^2 + 4k_j k_f M^*} - k_f (2n_c - 1)}{2k_j}. \quad (7)$$

The dynamical trajectories leading to the state  $(M^*, N^*)$  provide predictions for the self-assembly kinetics. These trajectories can be obtained analytically in an approximate form (assuming small  $k_f$  and sufficiently large  $N_0$ ), or using numerical simulations, both of which are described in the following sections. A summary of the solutions to the fibrillar growth kinetic model involving end-to-end joining under different initial conditions is provided in Table 1.

### Analytical solution for the self-assembly kinetics of a model including monomer addition, fragmentation, and end-joining

An approximate solution for the system of Eqs. 4 and 5 can be obtained in closed form using the following method, for the choice of parameters for

**TABLE 1** Summary of solutions to fibrillar growth kinetic models involving end-to-end joining

Model	Solution	Comments
$dM/dt = 2k_+(m_{\text{tot}} - M)N$ $dN/dt = -k_j N^2$	$M(t) = m_{\text{tot}} - \frac{m_{\text{tot}} - M_0}{(1 + k_j N_0 t)^{2k_+/k_j}}$	exact solution for the fibrillar mass density $M(t)$
	Eq. 18	exact implicit solution $N(M)$ , valid for any combination of parameters
$dN/dt = k_f M - k_j N^2$ $dM/dt = 2k_+(m_{\text{tot}} - M)N$	$M(t) = m_{\text{tot}} - \frac{m_{\text{tot}} - M_0}{1 - \frac{M_0}{m_{\text{tot}}} + \frac{M_0}{m_{\text{tot}}} \cosh(2k_+ N^* t) + \frac{N_0}{N^*} \sinh(2k_+ N^* t)}$	exact solution for $M(t)$ , valid when $k_j = 2k_+$
	Eq. 16	approximate solution for $M(t)$ , valid when the kinetics are reminiscent of decay profiles, lacking a measurable lag phase

$M$  is the concentration of monomer incorporated in fibrils (fibril mass density) at any time;  $N$  is the concentration of fibrils (number density);  $M_0$  is the initial fibril mass density;  $N_0$  is the initial number density of fibrils;  $m_{\text{tot}}$  is the total monomer density;  $N^* \approx \sqrt{k_f m_{\text{tot}}/k_j}$  is the equilibrium number density of fibrils;  $k_+$  is the linear growth rate constant;  $k_j$  is the end-joining rate constant; and  $k_f$  is the fibril fragmentation rate constant.

which  $m(t)$  does not develop a sigmoidal shape; a closed form solution for the case where  $m(t)$  develops a sigmoidal shape has been obtained very recently in Michaels and Knowles (35).

First, it is useful to define  $m = M/M^*$  and  $n = N/N^*$ , so that the equation is now expressed in terms of the dimensionless ratio of fibril mass and number density relative to their steady-state values. After rescaling the time variable  $\tau = 2k_+ N^* t$ , and assuming  $k_f \ll k_+ m_{\text{tot}}$  and  $k_f \ll k_j m_{\text{tot}}$ , the system from Eqs. 4 and 5 can be written as

$$\begin{aligned} \frac{dm}{d\tau} &= (1 - m)n, \\ m(0) &= M_0/M^* = m_0, \end{aligned} \quad (8)$$

$$\begin{aligned} \frac{dn}{d\tau} &= -rn^2 + r - r(1 - m_0)e^{-\tau}, \\ n(0) &= n_0. \end{aligned} \quad (12)$$

This equation can be solved (see the [Supporting Material](#) for details) as

$$n(\tau) = \frac{u}{4r} \frac{c[J_{2r+1}(u) - J_{2r-1}(u)] + Y_{2r+1}(u) - Y_{2r-1}(u)}{cJ_{2r}(u) + Y_{2r}(u)}, \quad (13)$$

$$u = 2r\sqrt{1 - m_0}e^{-\tau/2}, \quad (14)$$

$$c = \frac{Y_{2r-1}(2r\sqrt{1 - m_0}) - Y_{2r+1}(2r\sqrt{1 - m_0}) + \frac{2n_0}{\sqrt{1 - m_0}} Y_{2r}(2r\sqrt{1 - m_0})}{J_{2r-1}(2r\sqrt{1 - m_0}) - J_{2r+1}(2r\sqrt{1 - m_0}) + \frac{2n_0}{\sqrt{1 - m_0}} J_{2r}(2r\sqrt{1 - m_0})}, \quad (15)$$

$$\begin{aligned} \frac{dn}{d\tau} &= -rn^2 + rm, \\ n(0) &= N_0/N^* = n_0, \end{aligned} \quad (9)$$

where  $r \equiv k_f/(2k_+)$  is the ratio of the end-joining to the elongation rate constants. Equation 8 can be integrated yielding an expression for  $m(\tau)$  given an expression for  $n(\tau)$  of

$$m(\tau) = 1 - (1 - m_0)e^{-\int_0^\tau d\tau' n(\tau')}. \quad (10)$$

At late times  $n \approx 1$ , yielding

$$m(\tau|n \rightarrow 1) = 1 - (1 - m_0)e^{-\tau}, \quad (11)$$

$m(\tau|n \rightarrow 1)$  is a monotonically increasing, concave function and thus may serve as a good approximation to  $m(\tau)$  at early times, provided  $m(\tau)$  does not develop a sigmoidal shape. Using this expression as an approximation for  $m(\tau)$  at early times, we obtain the following nonlinear first-order ordinary differential equation for  $n(\tau)$ :

with  $J_\alpha(x)$  and  $Y_\alpha(x)$  being Bessel functions of the first and second kind, respectively. Equation 13 can be integrated and combined with Eq. 10 to obtain the approximation for  $m(\tau)$ ,

$$\begin{aligned} m(\tau) &= 1 - (1 - m_0) \\ &\times \left( \frac{cJ_{2r}(2r\sqrt{1 - m_0}) + Y_{2r}(2r\sqrt{1 - m_0})}{cJ_{2r}(2r\sqrt{1 - m_0}e^{-\tau/2}) + Y_{2r}(2r\sqrt{1 - m_0}e^{-\tau/2})} \right)^{1/r}, \end{aligned} \quad (16)$$

where the constant  $c$  is as defined in Eq. 15. Plots of the approximate solution given by Eqs. 13 and 16 are shown in [Fig. S9](#) along with curves generated numerically; clearly, the agreement between them is excellent.

An expression relating  $m$  and  $n$  may also be derived from Eqs. 8 and 9:

$$n \frac{dn}{dm} = -\frac{r}{1 - m} n^2 + \frac{rm}{1 - m}. \quad (17)$$

This is solvable for any  $n_0$ ,  $r$ , and  $m$ :

$$n(m) = \begin{cases} \left[ \left( n_0^2 - \frac{2rm_0 - 1}{2r - 1} \right) \left( \frac{1 - m}{1 - m_0} \right)^{2r} + \frac{2rm - 1}{2r - 1} \right]^{1/2}, & r \neq 1/2, \\ \left[ (n_0^2 - 1) \frac{1 - m}{1 - m_0} + (1 - m) \ln \frac{1 - m}{1 - m_0} + 1 \right]^{1/2}, & r = 1/2. \end{cases} \quad (18)$$

This is an exact implicit solution that relates the fibril number and fibril mass densities.

### Simulation of the self-assembly process including end-joining

Kinetic (stochastic) Monte Carlo simulations were performed by implementing a Gillespie algorithm using FORTRAN 95 and then by averaging over 150 replicate simulations for each set of conditions. The number of loops and fibrils were tracked for each length, along with the total monomer population  $m(t)$ . Length distributions were obtained at points in the simulation where the total fibril mass had reached a specific threshold (i.e., instead of at particular points in time).

## RESULTS AND DISCUSSION

### Heat treatment of reduced OVA produces fibrillar aggregates and closed loops with amyloidlike Congo Red and Thioflavin T binding properties

Incubation of reduced (10 mM DTT) OVA for several hours at 60°C at near-neutral pH (10 mM ammonium acetate, pH 6.8) produced species that bound Congo Red (see Fig. S1) and Th T. Examination of the heated OVA samples by TEM revealed the presence of fibrillar aggregates (Fig. 2, A–C). The fibrils formed by reduced OVA under these conditions are flexible with a persistence length of ~26 nm (see Fig. S2). The fibrils often appeared to be entangled, particularly at higher protein concentrations, a feature that prevents an accurate determination of their length distribution. Interestingly, our TEM images often reveal the formation of loops, in which the two ends of a single fibril appear to be annealed. Loops were observed in TEM images of heat-treated samples at both low (0.4 mg/mL) and high (6.4 and 12.8 mg/mL) initial concentration of protein (Fig. 2, A–D). The presence of loops in the samples provides clear evidence that fibrils of length greater than the persistence length can join end-to-end. Analysis of images from samples in which loop formation was abundant (80°C, 6.4 mg/mL) showed that the length distribution of fibrils in loops is centered at 120 nm, but skewed toward longer loops (loops as large as 360 nm in circumference could be seen; see histogram in Fig. 2 E). No loops were seen with circumference smaller than twice the persistence length, the smallest measured loop having a length of 74 nm.

### The kinetics of OVA self-assembly

The self-assembly kinetics of reduced OVA differ strongly from the standard sigmoidal behavior, and can be divided into three regimes (Fig. 3 A). In our experiments, fibril mass, as measured by the Th T fluorescence, increases sharply from the start of the experiment, with no apparent

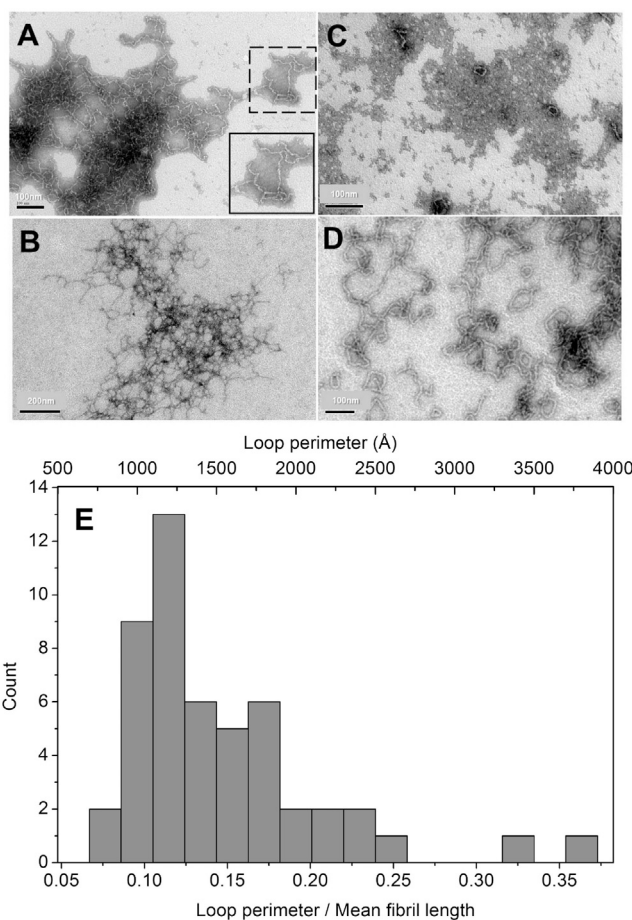


FIGURE 2 TEM images of fibrils formed by OVA. (A) Entangled and branched fibrils formed by 0.4 mg/mL OVA heated at 60°C. (Inset) Example of a branched fibril. (B) Entangled and branched fibrils formed by 12.8 mg/mL OVA heated at 60°C. (C) Loops formed by 0.4 mg/mL OVA fibrils at 60°C. (D) Loops formed by 6.4 mg/mL OVA fibrils at 80°C. (E) Experimental length distributions of OVA (6.4 mg/mL, incubated at 80°C) loops. For additional TEM images of loops and branches, see Figs. S4 and S5.

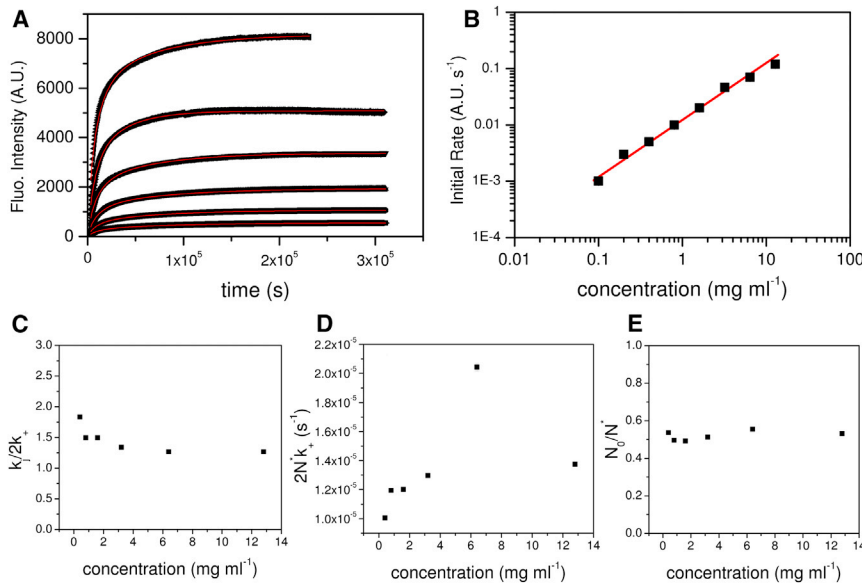


FIGURE 3 OVA self-assembly kinetics monitored by thioflavin T binding. (A) Kinetic traces of Th T binding by OVA between 0.4 and 12.8 mg/mL. (Symbols) Experimental data; (red solid lines) fitted curves according to Eq. 16. (B) Log-log plot of the initial growth rate versus concentration (red line represents a linear scaling relation). (C) Concentration dependence of the ratio of end-joining and growth rate constants. Interestingly, this factor decreases with concentration, possibly reflecting the lower diffusivity of the initial seed population in concentrated mixtures (which may arise because the effect of fibril length on growth is not taken into account by the model). (D) Concentration dependence of the timescaling factor  $2k_+N^*$ . While this factor increases with concentration, the observed dependence is much weaker than the one predicted from the theory (Eq. 7). (E) Concentration dependence of the ratio  $N_0/N^*$ . Because  $N^*$  is only weakly dependent on concentration, a constant ratio of  $N_0/N^* \approx 0.5$  predicts that  $N_0$  is concentration-independent, a necessary condition for the model to be consistent with the linear concentration scaling of the initial rate (B). To see this figure in color, go online.

lag phase (although at very early times, our measurements are obscured by a transient behavior that we attribute to temperature fluctuations). This initial growth phase is followed by a second growth regime, where the Th T fluorescence continues to increase but considerably more slowly, after which, the Th T fluorescence reaches a plateau.

The absence of a lag phase suggests that fibril formation in our experiments does not proceed via a classic homogeneous nucleation and growth mechanism by monomer addition. This interpretation is supported further by measurements of the relationship between protein concentration and the initial growth rate (Fig. 3 B). For a mechanism involving homogeneous nucleation and growth, one would expect that the initial aggregation rate, in the absence of seeds, to be equal to the initial nucleation rate, which can be assumed to scale as [protein concentration] <sup>$n_c$</sup>  (for rate-limited reactions),  $n_c \geq 2$  being the size of the nucleus. However, as shown in Fig. 3 B, in our experiments the initial aggregation rate scales linearly with protein concentration, suggesting that a process other than homogeneous nucleation must give rise to the initial population of growth-competent species. We also noticed that the initial aggregation rate was influenced by the material of the vessel in which our experiments were performed, with aggregation in microplates coated with a PEG-like polymer occurring substantially faster than in uncoated plates (see the Supporting Material for details). The initial aggregation rate also depends on the volume of the sample, with samples with a smaller surface area to volume ratio exhibiting less growth (see Fig. S6, D and E). These findings suggest that fibril growth is seeded at the walls of the sample container. For seeded growth, the initial growth rate is controlled by the initial monomer addition rate, which scales linearly with

number of seeds and protein concentration. If the surface is saturated with fibril seeds, then the number of seeds is independent of protein concentration, which would give rise to the observed linear scaling of the initial rate with protein concentration.

### Theoretical analysis of the model for fibril formation by linear growth, end-joining, and fragmentation

Results for the theoretical trajectories of the model described by Eqs. 8 and 9 reveal qualitatively different types of dynamical behavior, depending on the parameters—in particular on the initial concentration of seed fibrils  $N_0$  (see the phase diagram shown in Fig. 4 A).

For small seed density  $N_0 \ll N^*$  (i.e., if the initial concentration of seeds is much smaller than the long-time fibril density), the model predicts sigmoidal kinetics for the fibril mass  $M$ . In this case, the only apparent effect of end-joining is to smooth out the transition between the rapid growth phase and the plateau (Fig. 4, B and C,  $n_0 = 0.001$ ). By taking the kinetics of the fibril number density  $N(t)$  into account, we may distinguish two cases: if the end-joining rate constant is much less than the elongation rate constant, i.e.,  $k_j \ll 2k_+$ ,  $N(t)$  increases slowly as the bulk of the free protein aggregates, increasing sharply to its long-time value during the late stages of the process (Fig. 4 C,  $r = 0.1$ ). When  $k_j$  is comparable to or greater than  $2k_+$ ,  $N(t)$  follows a sigmoidal form similar to  $M(t)$  (Fig. 4 C,  $r = 2$ ).

Contrasting behavior is predicted by the model if the initial seed concentration is sufficiently high. In this case, the model predicts rapid fibril growth from the start, with no lag phase (Fig. 4 B,  $n_0 = 1.5$ ). For a small end-joining

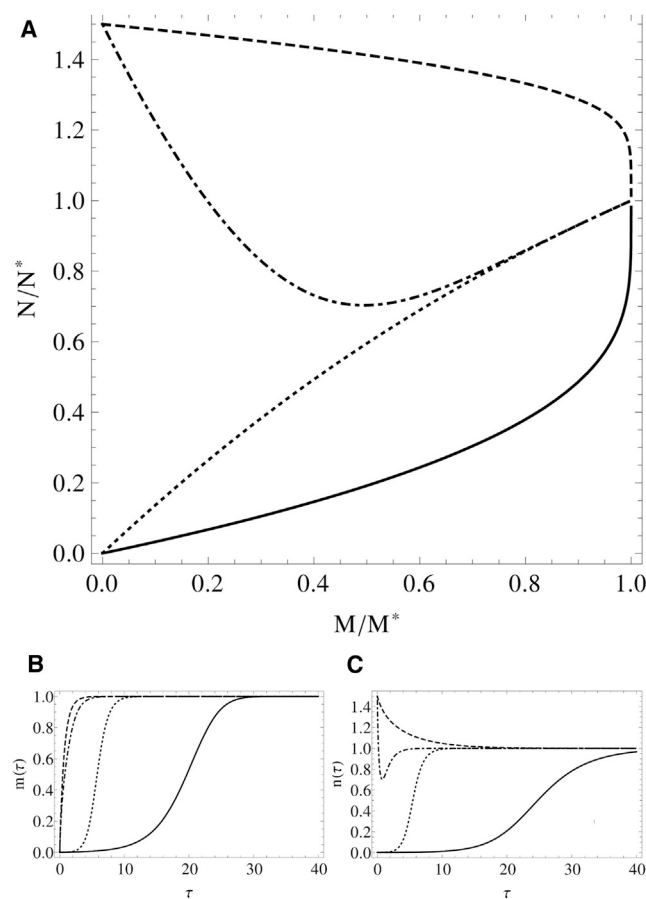


**FIGURE 4** Theoretical trajectories of the model described by Eqs. 8 and 9. (A) Phase diagram of the system showing four distinct types of dynamics: (solid line) small initial seed population and small end-joining rate ( $n_0 = 0.001$ ,  $r = 0.1$ ); (dotted line) small initial seed population and end-joining rate comparable to elongation ( $n_0 = 0.001$ ,  $r = 2$ ); (dashed line) high initial seed population and low end-joining rate ( $n_0 = 0.001$ ,  $r = 0.1$ ); and (dot-dashed line) high end-joining rate and high initial seed population ( $n_0 = 1.5$ ,  $r = 2$ ). The dynamics of the normalized fibril mass density  $m$  and the normalized fibril number density  $n$  for these four cases are shown in panels (B) and (C), respectively. When the end-joining rate constant is comparable to the elongation rate constant and the initial seed concentration is also high, fibril growth sites are depleted at early times due to end-joining of fibril ends before they begin increasing again at later times as a result of fibril breaking; this fluctuation generates a characteristically delayed equilibration of the fibrillar mass fraction growth curve.

rate  $k_j \ll 2k_+$ ,  $M(t)$  shows a single growth phase, ending in a plateau, while  $N(t)$  decays monotonically to its long-time value  $N^*$  (Fig. 4, B and C,  $r = 0.1$ ). Interestingly however, if the end-joining rate constant is significant ( $k_j \approx 2k_+$ ), the model predicts two distinct fibril growth phases: the fibril mass concentration  $M(t)$  initially grows rapidly, followed by a slower growth phase, before it eventually reaches a plateau. This behavior is correlated with the kinetics of the fibril number  $N(t)$ , which is nonmonotonic:  $N(t)$  decreases during the initial growth phase, overshoots its long-time value  $N^*$ , and gradually increases toward  $N^*$  during the second fibril growth phase (Fig. 4 C,  $r = 2$ ).

The biphasic aggregation kinetics predicted by the model is strikingly similar to our experimental observations for OVA. Therefore, the model leads us to suggest not only that both fragmentation and end-joining are important for OVA, but also that in our experiments self-assembly starts with a large number of short but growth-competent species, which due to their small size may still represent a very small proportion of the total mass fraction. The model also predicts that the absolute number of fibrils in our experiments (as opposed to the fibril mass) actually decreases in time from its initially high value, before again increasing.

Thus our theoretical analysis suggests that the kinetics observed in our experiments reflect the interplay between the two competing processes of fragmentation (which creates new growth-competent ends) and end-joining (which decreases the number of fibril ends). Initially, growth proceeds rapidly from a seed population that consists of numerous small species. Later, a relatively high rate of end-joining depletes the number of fibril ends to which free monomers may attach: this process is manifested by the decrease in the growth rate that is evident in the second observed growth phase. Finally, a small fibril breakage rate eventually ensures there are enough ends for the remaining free monomers to attach to, bringing the fibril growth process to completion.

### Experimental confirmation of the growth pathway

Fitting our experimental Th T fluorescence curves for ovalbumin (Fig. 3) using our analytical formula (Eq. 16) for the self-assembly kinetics including end-joining and fragmentation allows us to estimate the relevant kinetic parameters (Fig. 3, C–E). The initial number density of fibril seeds (i.e., growth-competent species) is indeed estimated to be high ( $N_0/N^* \approx 0.5$ , Fig. 3 E), but these seeds nonetheless represent only a very small proportion of the total amount of protein present ( $M_0 \ll m_{\text{tot}}$ ). Interestingly, the rate constants for elongation and end-joining are of similar magnitude (Fig. 3 C), suggesting that end-joining is of comparable importance to the kinetics. As can be seen in Fig. 3 D, the timescale factor  $2k_+N^*$  increases with concentration, but the observed dependence is weaker than predicted from the theory (Eq. 7). This, together with the observation that the ratio  $N_0/N^*$  is a constant (Fig. 3 E), implies that  $N_0$  is concentration-independent and is consistent with our previous argument that fibril seeds are saturated at surfaces.

Having all the relevant parameters in hand, we can perform a simulation of the model using the parameters derived from fitting of the experimental data, which allows us to monitor evolution of a species over time. Due to the high number of fibrils forming early during polymerization, we observe loops forming rapidly during the early stages (Fig. 5 A), and then increasing at a diminishing rate. This gives rise to a loop length distribution that increases fairly

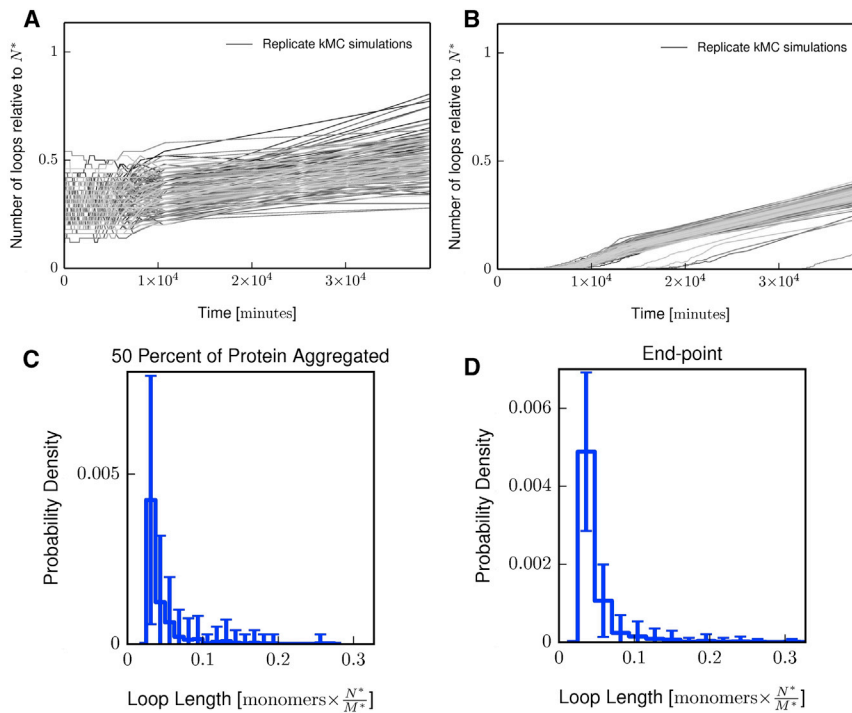


FIGURE 5 The dynamics for the loop number fraction generated by stochastic simulations for (A) heavily seeded growth and (B) for a case exhibiting sigmoidal kinetics. We find that the number of loops is established early in the kinetics for highly seeded growth. This is in contrast to low initial seed concentrations where the appearance of loops does not happen until further into the growth kinetics and does not reach an appreciable number until late times. (C) Simulated loop perimeter distribution at the midpoint; (D) simulated loop perimeter distribution at the end-point. Both simulated distributions are normalized to the average fibril length at equilibrium. Note that  $N^*/M^*$  scales as the inverse mean fibril length. Therefore, the simulation loop length is scaled by the mean stationary fibril length and gives an indication of how long the loops are relative to this mean value. To see this figure in color, go online.

sharply at lengths  $>2l_p$  and then decays more slowly with increasing loop length (Fig. 5, C and D). The length distribution for loops is thus qualitatively similar to the one observed experimentally, i.e., peaked but with a long tail (Fig. 2 E). This loop perimeter distribution is established early (when  $<50\%$  of the starting material has aggregated) and does not change significantly over time. Therefore, it may be expected that in systems with flexible fibrils with sufficiently high initial seeding species the loop population will have formed after the initial growth phase and remain intact until the process is completed. This situation can be contrasted with the curves displaying sigmoidal kinetics (resulting from small initial seed concentrations) where loops only appear after some lag-time and only reach an appreciable number when the self-assembly process is almost complete (Fig. 5 B). The model studied in this article therefore provides a framework for predicting when different fibril morphologies arise.

It is also worth commenting on the observation that OVA fibrils exhibit branched morphologies (Fig. 2 A inset; see also Fig. S5). We can show that these branches do not form by fibrils overlapping on the surface of the TEM grid as an artifact of the deposition process, by analyzing the angular distribution of the fibril branches (Fig. S7). Such branching may occur via two different mechanisms: heterogeneous nucleation at a fibril surface or joining of an existing fibril end to the body of another fibril. Kinetically, these processes are distinct. Heterogeneous nucleation will be a source of new fibril ends, whereas annealing of an existing fibril end to the body of another fibril will act as a sink by consuming one growth-competent end. Our kinetic

analysis is consistent with a model where fibril ends are depleted rather than created during the aggregation process, suggesting that the joining of an existing fibril to the body of another occurs during OVA self-assembly under these conditions.

The fact that the rate constants for elongation and end-joining are of similar magnitude suggests that the ends behave analogously to free-floating monomers. This may suggest that joining of fibril ends and elongation have similar activation barriers. Such a result is plausible because both processes involve protein-protein assembly.

Analysis of OVA fibril growth kinetics at different temperatures supports this hypothesis (Fig. 6, A–C). The T fluorescence during the assembly of OVA at a concentration of 6.0 mg/mL was recorded at six different temperatures (50, 55, 60, 65, 70, and 80°C). As expected, the fibril formation process is accelerated at higher temperatures. Arrhenius plots show that the ratio  $r = k_j/(2k_+)$  (see Materials and Methods) remains essentially constant with temperature (Fig. 6 C), suggesting that end-joining and elongation have similar activation barriers. This result can easily be understood by first assuming an Arrhenius-like form for the relevant rate constants, i.e.,  $k_j = Ae^{-(E_j^\ddagger/RT)}$  and likewise for  $k_+$ . Because our experiments have shown that

$$\frac{d(\ln r)}{d(1/RT)} \approx 0,$$

it follows then that  $E_j^\ddagger \approx E_+^\ddagger$ . Conversely,  $2k_+N^*$  does display Arrhenius behavior (Fig. 6 B). Because, for

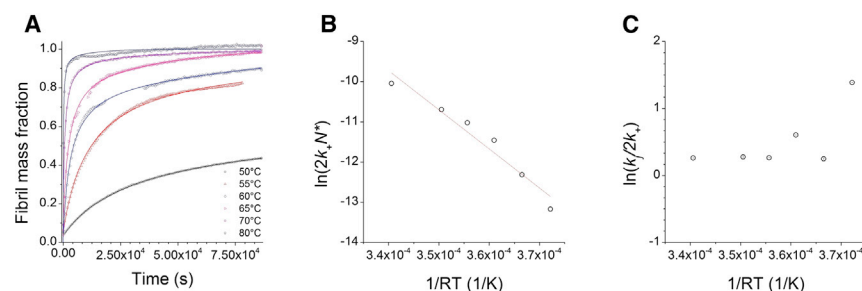


FIGURE 6 (A) Kinetic traces of Th T binding by 6.0 mg/mL OVA at 50 (black circles), 55 (red triangles), 60 (blue diamonds), 65 (green crosses), 70 (purple squares), and 80°C (pink asterisks). (Symbols) Experimental data; (black solid lines) fitted curves. (B) Arrhenius plot for the timescaling factor  $2k_+N^*$  for 6.0 mg/mL OVA. (C) Arrhenius plot for the  $k_f/(2k_+)$  ratio for 6.0 mg/mL OVA. Clearly the latter does not exhibit typical Arrhenius behavior, indicating that end-joining and elongation have similar energy barriers. To see this figure in color, go online.

$k_f \ll k_+, k_j$ , the value  $N^*$  can be approximated by  $(m_{\text{tot}}k_f/k_j)^{1/2}$ , the gradient of the Arrhenius plot is

$$\frac{d(\ln[2k_+N^*])}{d(1/RT)} \approx -E_+^\ddagger - \frac{1}{2}E_f^\ddagger + \frac{1}{2}E_j^\ddagger,$$

where  $E^\ddagger$  represents activation energies for each process. The energy barrier obtained from Fig. 6 B is 97.2 kJ/mol. The similarities of the energy barriers for end-joining and fibril growth are interesting and may point to these two processes being mechanistically similar, i.e., that a strong parallel may exist between monomer addition at a growth site and the coalescence of two fibril growth sites. Moreover, because the polymerization rate changes visibly over the temperature range studied (as evidenced by Fig. 6 A), the energy barrier ought to be comparable to  $RT$  at that temperature range (2.7–3.1 kJ/mol), assuming that these processes are rate-limited. Thus, by far the major contribution to the value obtained from Fig. 6 B must originate from the fragmentation process. These considerations lead to an estimate of 191.2–191.8 kJ/mol for  $E_f^\ddagger$ , which is high compared to  $RT$ , a result that is entirely consistent with the initial assumption that fragmentation is a slow process. The initial fibrillar mass fraction does not display any trend as a function of temperature—indeed, the fits allow significant variation for this parameter, given that it is a small number. Notably, temperature does affect the initial seed density with higher temperatures giving rise to a higher initial seed concentration; thus, whatever the seeding process is, it is temperature-dependent. Nevertheless, even samples incubated at 50°C do not display a measurable lag phase, indicating that the initial number of seeds never falls below the threshold value required for an appreciable lag phase to be observed. It is worth noting that, while we have fit a straight line to Fig. 6 B, we cannot rule out that the data exhibits nonlinear, convex Arrhenius behavior. Such complex temperature dependence has been previously observed in the kinetics of certain enzyme reactions and has been ascribed to partial inhibition (loss of reactant species) at higher temperatures (36). Our data could be consistent with either the loss of reactants, through denaturation of seeds or monomeric protein in the conformation suitable for elongation, or a decrease in the apparently large energy barrier required for fragmentation. Nonetheless, both the

kinetic data and the temperature dependence taken together are consistent with fragmentation being slower (and having a higher energy barrier) than the other processes.

### The effect of end-joining on self-assembly dynamics and implications for amyloid-like fibril growth

Our model of ovalbumin self-assembly establishes a link between subtle features of the aggregation kinetics and the molecular processes underlying self-assembly: in this case the joining between fibril ends. Such processes give rise to the formation of nano- and microscale structures with intriguing morphologies (e.g., loops). Such a model can also be enlisted to interpret a far wider array of self-assembly phenomena. In the limit of a vanishing end-joining term and a low seed concentration, the kinetics approach the nucleation, growth, and fragmentation model, which begins with a lag phase but is followed by fast growth, equilibrating rapidly due to its autocatalytic nature (8,9). Polymerization with low initial seed concentration and an end-joining term that effectively cancels out a small fragmentation term qualitatively resembles the classical nucleation-and-growth case, characterized by a short lag phase followed by a growth phase but with slow equilibration (37). When the end-joining term is sufficiently high it will effectively inhibit the polymerization process by removing elongation sites. By counteracting the effects of fibril fragmentation, inclusion of end-joining gives rise to kinetic curves that can have either abrupt (small end-joining rate constant) or slow (large end-joining rate constant) equilibration after the growth phase.

The fibril length distribution at late times resulting from this case is exponential, a hallmark of polymer fragmentation (38), but significantly broadened, indicating that end-joining dynamically stabilizes large aggregates (see Fig. S3 B). Thus the simple inclusion of an end-joining term to the equations describing linear polymerization and fibril breaking can significantly improve the quantitative understanding of protein fibrillization (and other similar polymerization reactions) as well as describing processes, such as those observed for OVA, which cannot be accounted for without it. For completeness, we compare our model

with two recent models that specifically take into account end-joining (35,39). Yang et al. (39) studied an equilibrium model for linear and closed-loop formation, deriving rate equations for monomers (depletion) and the concentration of an average fibril, which were then solved numerically using the rate constants inferred from equilibrium measurements. In our work we are not treating the system in equilibrium, mainly because it is uncertain whether these systems ever truly reach equilibrium due to gelation or other mechanisms of kinetic arrest. Instead, we fit the kinetics to the analytical model to obtain rate constants, rather than obtaining them from the equilibrium state. We believe this method provides a better route in obtaining the various kinetic parameters of the system. More recently, Michaels and Knowles (35) studied a kinetic model similar to ours that, compared to our model, includes several other reactions to satisfy microscopic reversibility. However, their theoretical analysis pertains to the aggregation in the absence of preformed seed aggregates, and is thus not directly applicable to our experiments.

The model described by Eqs. 4 and 5 and its solutions (Eq. 16 as well as Eqs. S22 and S35 in the [Supporting Material](#)) can be used to reveal whether end-joining and fragmentation contribute significantly to a fibrillization process based on the aggregation kinetics. In doing so, several new questions are opened up. What are the molecular processes that allow end-joining to occur, which may explain the apparent values of the rate constants? The fact that the systems under question grow linearly into fibrils implies that there exists a preferred direction for growth (at least once a sufficiently large oligomer has already formed); but can anything be said about the arrangement of the peptides in the fibril core? In straight amyloid-like fibrils, peptide strands are thought to exist in a highly ordered, quasi-crystalline state (40,41). Such an arrangement limits the number of orientations in which another fibril end may dock to an existing end, unless monomers at fibril ends initially have a different configuration before they adopt that of the fibril interior. Alternatively, the interface between monomers in a fibril may exhibit some structural heterogeneity, which might, in turn, explain not only high end-joining and elongation rates but also the flexibility of the resulting fibers, observed for OVA and other aggregating proteins (42–44). Thus, end-joining (and possibly elongation) must either be a multistep process (dock-and-lock), or a certain degree of structural variability should be expected along the fibril.

The mechanism of loop formation in this work occurs by virtue of the intrinsic flexibility of these wormlike fibrils. We have estimated the persistence length of these fibrils to be 26 nm (Fig. S2). Accordingly, the average angle at which the tangential direction along the fibril becomes uncorrelated is  $\sim 1$  radian. A closed loop of  $2\pi$  radians must therefore have a diameter of at least  $\sim 150$  nm, which agrees well with the mean length of the fibrils in this

study  $\approx 230$  nm (Fig. S3 A). For long straight fibrils with much higher persistence length (on the order of microns or greater), the formation of such closed looped morphologies would be an energetically expensive process. Other mechanisms then must come into play in order to form such morphologies, as was recently highlighted by Jordens et al. (45).

Several proteins form polymorphic fibrils. Some form different fibril morphologies under different environmental conditions (such as in apo-C II (46),  $\alpha$ -syn (43,44),  $\beta$ -2m (18), and OVA (47,48)). Alternatively some, like A $\beta$ , form flexible, wormlike fibrils early in the aggregation process before the appearance of rigid fibrils (9). As with OVA, in several other cases end-joining is implied by the presence of loops (21–27). Notably, aggregation leading to the formation of wormlike fibrils will often either exhibit a short lag phase, or not exhibit a lag phase at all, indicating that the process giving rise to the critical concentration of growth-competent species is rapid: is this situation brought about by the inherent stability of the nucleus for wormlike fibrils or is it a result of wormlike fibrils being able to grow from a heterogeneous mix of monomer conformations?

Another question, of relevance to the role of amyloid-like fibrils in disease, concerns the toxicity of the fibril population resulting from this mechanism (which has also been raised by Hatters et al. (21)). In the long-time limit, assuming that the fibrils do not undergo any further rearrangements, the fibril length distribution will be broad but exponential. For flexible fibrils, and even with the inclusion of fibril fragmentation, small loops will be present from the initial growth phase onwards (Fig. 5). The consequences of such a fibril length distribution are determined by which species are cytotoxic. Shorter fibrils formed by fragmentation of larger amyloid fibrils have been found to be more cytotoxic for a number of systems, including  $\alpha$ -synuclein (49). If protein oligomers or short fibrillar aggregates are the toxic species, loop formation would be desirable because it would act as a protective sink, locking away the constituent proteins in an inert state for an extended time. Loops formed early in the aggregation process will be stable because they cannot grow any further, and their breaking is relatively infrequent due to their small length (which limits the number of possible breakage sites). Thus, a method of inducing fibril end-joining would delay the accumulation of toxic species.

Alternatively, it has been proposed that annular morphologies observed in A $\beta$  (1-40) and  $\alpha$ -synuclein (22) are reminiscent of a class of pore-forming bacterial toxins that can disrupt cellular membranes (50). If these structures are indeed toxic, loop formation would result in a long-lived population of harmful morphological species. More work needs to be done to characterize the role of circularized morphologies in cellular toxicity. Ultimately, relating fibril morphology to the growth pathway can contribute to rationalizing therapeutic strategies for amyloidoses.

## SUPPORTING MATERIAL

Supporting Materials and Methods, Supporting Results, and ten figures are available at [http://www.biophysj.org/biophysj/supplemental/S0006-3495\(15\)00282-9](http://www.biophysj.org/biophysj/supplemental/S0006-3495(15)00282-9).

## AUTHOR CONTRIBUTIONS

J.M.D.K. designed experiments, performed experiments, analyzed data, and wrote the article. J.S.-N. built and solved the mathematical model and wrote and edited the article. R.J.M. designed experiments, performed experiments, analyzed data, wrote, and edited the article. K.E. designed, performed, and analyzed stochastic simulations. S.C., S.T., and J.G. performed both experiments and data analysis. P.E.B., R.J.A., and C.E.M. designed the research and edited the article.

## ACKNOWLEDGMENTS

J.S.-N., R.J.M., and C.E.M. acknowledge funding from the Engineering and Physical Sciences Research Council under grant No. EP/J007404/1. J.M.D.K., P.E.B., and C.E.M. also acknowledge funding by the Biotechnology and Biological Sciences Research Council under grant No. BB/C00759X/2. R.J.A. was supported by a Royal Society University Research Fellowship.

## REFERENCES

- Chiti, F., and C. M. Dobson. 2006. Protein misfolding, functional amyloid, and human disease. *Annu. Rev. Biochem.* 75:333–366.
- Cherny, I., and E. Gazit. 2008. Amyloids: not only pathological agents but also ordered nanomaterials. *Angew. Chem. Int. Ed. Engl.* 47:4062–4069.
- Channon, K., and C. E. MacPhee. 2008. Possibilities for ‘smart’ materials exploiting the self-assembly of polypeptides into fibrils. *Soft Matter.* 4:647–652.
- Goldschmidt, L., P. K. Teng, ..., D. Eisenberg. 2010. Identifying the amyloids, proteins capable of forming amyloid-like fibrils. *Proc. Natl. Acad. Sci. USA.* 107:3487–3492.
- Vassar, P. S., and C. F. Culling. 1959. Fluorescent stains, with special reference to amyloid and connective tissues. *Arch. Pathol.* 68:487–498.
- Saeed, S. M., and G. Fine. 1967. Thioflavin-T for amyloid detection. *Am. J. Clin. Pathol.* 47:588–593.
- Naiki, H., K. Higuchi, ..., T. Takeda. 1989. Fluorometric determination of amyloid fibrils in vitro using the fluorescent dye, thioflavin T1. *Anal. Biochem.* 177:244–249.
- Cohen, S. I. A., M. Vendruscolo, ..., T. P. J. Knowles. 2011. Nucleated polymerization with secondary pathways. II. Determination of self-consistent solutions to growth processes described by non-linear master equations. *J. Chem. Phys.* 135:065106.
- Cohen, S. I. A., M. Vendruscolo, ..., T. P. J. Knowles. 2011. Nucleated polymerization with secondary pathways. I. Time evolution of the principal moments. *J. Chem. Phys.* 135:065105.
- Knowles, T. P. J., C. A. Waudby, ..., C. M. Dobson. 2009. An analytical solution to the kinetics of breakable filament assembly. *Science.* 326:1533–1537.
- Goldsbury, C. S., G. J. Cooper, ..., J. Kistler. 1997. Polymorphic fibrillar assembly of human amylin. *J. Struct. Biol.* 119:17–27.
- Goldsbury, C. S., S. Wirtz, ..., P. Frey. 2000. Studies on the in vitro assembly of a  $\beta$  1-40: implications for the search for a  $\beta$ -fibril formation inhibitors. *J. Struct. Biol.* 130:217–231.
- Lashuel, H. A., S. R. Labrenz, ..., J. W. Kelly. 2000. Protofilaments, filaments, ribbons, and fibrils from peptidomimetic self-assembly: implications for amyloid fibril formation and materials science. *J. Am. Chem. Soc.* 122:5262–5277.
- Lara, C., J. Adamcik, ..., R. Mezzenga. 2011. General self-assembly mechanism converting hydrolyzed globular proteins into giant multi-stranded amyloid ribbons. *Biomacromolecules.* 12:1868–1875.
- Adamcik, J., V. Castelletto, ..., R. Mezzenga. 2011. Direct observation of time-resolved polymorphic states in the self-assembly of end-capped heptapeptides. *Angew. Chem. Int. Ed. Engl.* 50:5495–5498.
- Reches, M., and E. Gazit. 2003. Casting metal nanowires within discrete self-assembled peptide nanotubes. *Science.* 300:625–627.
- Rochet, J. C., and P. T. Lansbury, Jr. 2000. Amyloid fibrillogenesis: themes and variations. *Curr. Opin. Struct. Biol.* 10:60–68.
- Aggeli, A., M. Bell, ..., N. Boden. 2003. pH as a trigger of peptide  $\beta$ -sheet self-assembly and reversible switching between nematic and isotropic phases. *J. Am. Chem. Soc.* 125:9619–9628.
- Harper, J. D., C. M. Lieber, and P. T. Lansbury, Jr. 1997. Atomic force microscopic imaging of seeded fibril formation and fibril branching by the Alzheimer’s disease amyloid- $\beta$  protein. *Chem. Biol.* 4:951–959.
- Harper, J. D., S. S. Wong, ..., P. T. Lansbury. 1997. Observation of metastable A $\beta$  amyloid protofibrils by atomic force microscopy. *Chem. Biol.* 4:119–125.
- Hatters, D. M., C. A. MacRaid, ..., G. J. Howlett. 2003. The circularization of amyloid fibrils formed by apolipoprotein C-II. *Biophys. J.* 85:3979–3990.
- Conway, K. A., S. J. Lee, ..., P. T. Lansbury, Jr. 2000. Acceleration of oligomerization, not fibrillization, is a shared property of both  $\alpha$ -synuclein mutations linked to early-onset Parkinson’s disease: implications for pathogenesis and therapy. *Proc. Natl. Acad. Sci. USA.* 97:571–576.
- Meehan, S., T. P. Knowles, ..., J. A. Carver. 2007. Characterization of amyloid fibril formation by small heat-shock chaperone proteins human  $\alpha$ A-,  $\alpha$ B- and R120G  $\alpha$ B-crystallins. *J. Mol. Biol.* 372:470–484.
- Ecroyd, H., and J. A. Carver. 2009. Crystallin proteins and amyloid fibrils. *Cell. Mol. Life Sci.* 66:62–81.
- Juárez, J., P. Taboada, and V. Mosquera. 2009. Existence of different structural intermediates on the fibrillation pathway of human serum albumin. *Biophys. J.* 96:2353–2370.
- Jordens, S., J. Adamcik, ..., R. Mezzenga. 2011. Disassembly and reassembly of amyloid fibrils in water-ethanol mixtures. *Biomacromolecules.* 12:187–193.
- Thorn, D. C., H. Ecroyd, ..., J. A. Carver. 2008. Amyloid fibril formation by bovine milk  $\alpha$ s<sub>2</sub>-casein occurs under physiological conditions yet is prevented by its natural counterpart,  $\alpha$ s<sub>1</sub>-casein. *Biochemistry.* 47:3926–3936.
- Binger, K. J., C. L. L. Pham, ..., G. J. Howlett. 2008. Apolipoprotein C-II amyloid fibrils assemble via a reversible pathway that includes fibril breaking and rejoining. *J. Mol. Biol.* 376:1116–1129.
- Naeem, A., T. A. Khan, ..., M. Saleemuddin. 2011. A partially folded state of ovalbumin at low pH tends to aggregate. *Cell Biochem. Biophys.* 59:29–38.
- Sabaté, R., and J. Estelrich. 2002. Aggregation characteristics of ovalbumin in  $\beta$ -sheet conformation determined by spectroscopy. *Biopolymers.* 67:113–120.
- Haurowitz, F., F. Dimoia, and S. Tekman. 1952. The reaction of native and denatured ovalbumin with Congo Red. *J. Am. Chem. Soc.* 74:2265–2271.
- Veerman, C., G. de Schiffart, ..., E. van der Linden. 2003. Irreversible self-assembly of ovalbumin into fibrils and the resulting network rheology. *Int. J. Biol. Macromol.* 33:121–127.
- Kato, A., and T. Takagi. 1988. Formation of intermolecular  $\beta$ -sheet structure during heat denaturation of ovalbumin. *J. Agric. Food Chem.* 36:1156–1159.
- Tanaka, N., Y. Morimoto, ..., N. Takahashi. 2011. The mechanism of fibril formation of a non-inhibitory serpin ovalbumin revealed by the identification of amyloidogenic core regions. *J. Biol. Chem.* 286:5884–5894.

35. Michaels, T. C. T., and T. P. J. Knowles. 2014. Role of filament annealing in the kinetics and thermodynamics of nucleated polymerization. *J. Chem. Phys.* 140:214904.
36. Truhlar, D., and A. Kohen. 2001. Convex Arrhenius plots and their interpretation. *Proc. Natl. Acad. Sci. USA.* 98:848–851.
37. Oosawa, F., and M. Kasai. 1962. A theory of linear and helical aggregations of macromolecules. *J. Mol. Biol.* 4:10–21.
38. Cohen, S. I. A., M. Vendruscolo, ..., T. P. J. Knowles. 2011. Nucleated polymerization with secondary pathways. III. Equilibrium behavior and oligomer populations. *J. Chem. Phys.* 135:065107.
39. Yang, S., M. D. W. Griffin, ..., G. J. Howlett. 2012. An equilibrium model for linear and closed-loop amyloid fibril formation. *J. Mol. Biol.* 421:364–377.
40. Sawaya, M. R., S. Sambashivan, ..., D. Eisenberg. 2007. Atomic structures of amyloid cross- $\beta$  spines reveal varied steric zippers. *Nature.* 447:453–457.
41. Fitzpatrick, A. W., G. T. Debelouchina, ..., C. M. Dobson. 2013. Atomic structure and hierarchical assembly of a cross- $\beta$  amyloid fibril. *Proc. Natl. Acad. Sci. USA.* 110:5468–5473.
42. Kodali, R., and R. Wetzel. 2007. Polymorphism in the intermediates and products of amyloid assembly. *Curr. Opin. Struct. Biol.* 17:48–57.
43. Giehm, L., C. L. P. Oliveira, ..., D. E. Otzen. 2010. SDS-induced fibrillation of  $\alpha$ -synuclein: an alternative fibrillation pathway. *J. Mol. Biol.* 401:115–133.
44. Necula, M., C. N. Chirita, and J. Kuret. 2003. Rapid anionic micelle-mediated  $\alpha$ -synuclein fibrillization in vitro. *J. Biol. Chem.* 278:46674–46680.
45. Jordens, S., E. E. Riley, ..., R. Mezzenga. 2014. Adsorption at liquid interfaces induces amyloid fibril bending and ring formation. *ACS Nano.* 8:11071–11079.
46. Hatters, D. M., C. E. MacPhee, ..., G. J. Howlett. 2000. Human apolipoprotein C-II forms twisted amyloid ribbons and closed loops. *Biochemistry.* 39:8276–8283.
47. Weijers, M., K. Broersen, ..., R. W. Visschers. 2008. Net charge affects morphology and visual properties of ovalbumin aggregates. *Biomacromolecules.* 9:3165–3172.
48. Lara, C., S. Gourdin-Bertin, ..., R. Mezzenga. 2012. Self-assembly of ovalbumin into amyloid and non-amyloid fibrils. *Biomacromolecules.* 13:4213–4221.
49. Xue, W. F., A. L. Hellewell, ..., S. E. Radford. 2009. Fibril fragmentation enhances amyloid cytotoxicity. *J. Biol. Chem.* 284:34272–34282.
50. Lashuel, H. A., D. Hartley, ..., P. T. Lansbury, Jr. 2002. Neurodegenerative disease: amyloid pores from pathogenic mutations. *Nature.* 418:291.